



Broadband Airfoil-Noise Source Localization by Microphone Arrays and Modeling of a Swept Free-Tip Blade

Gyuzel R. Yakhina, * and Michel Roger †

*Univ Lyon, École Centrale de Lyon (Univ. de Lyon), Lab. de Mécanique des Fluides et Acoustique,
UMR CNRS 5509, 36 avenue Guy de Collongue, Ecully 69134, France*

Arthur Finez, ‡ and Valentin Baron §

MicrodB, 28 Chemin du Petit Bois, Ecully 69130, France

Stéphane Moreau, ¶

*Université de Sherbrooke, Depart. Génie Mécanique,
2500 Boulevard de l'Université, Sherbrooke, Quebec J1K2R1, Canada*

Justine Giez †

*Safran Aircraft Engines, Aerodynamics and Acoustics Department,
Rond-Point René Ravaud - Réau, Moissy-Cramayel 77500, France*

The present paper describes a post-processing methodology of microphone-array results for accurate source localization and separation. A deconvolution method CIRA is used to extract quantitative spectral results for multiple noise sources identified on a wall-mounted, finite-span swept and cambered airfoil tested in an open-jet aeroacoustic facility. This allows understanding the contribution of each source in the noise generation process. The total sound pressure level is reconstructed from the individual spectra of each noise source and extrapolated in the far field to be compared with a single-microphone spectrum. The Bayesian algorithm is used to improve the comparison between reconstructed and experimental spectra as it takes into account the coherent nature of the sources. Remaining discrepancies motivate a re-examination of the assumptions made in the post-processing, aimed at making the spectral characterization of extracted sources more accurate. For this, analytical models of the source mechanisms and of their spanwise correlation are proposed as a tool to define future improvements.

Introduction

In most experiments dedicated to airfoil noise investigation from far-field measurements using single microphones, typically in open-jet anechoic wind tunnels, two main issues are identified. Firstly the noise from the tested airfoil is contaminated by some background noise generally caused by the nozzle jet mixing and the interaction of the jet with other surfaces such as end-plates. Usually this background noise is assumed not correlated with the targeted airfoil noise and measured separately, so that it can be subtracted from the noise measured with the airfoil installed.^{1,2} This makes no extraction possible when airfoil noise is overwhelmed by the background noise and consequently reduces the frequency range of the investigation. Secondly airfoil noise itself is made of several contributions, such as turbulence-impingement noise at the leading edge,

*Post-doc

†Professor, Member CEAS

‡PhD, Acoustic engineer

§PhD candidate

¶Professor, Lifetime AIAA member

†PhD candidate

trailing-edge noise, tip-vortex associated noise and possibly leading-edge vortex-induced noise.^{3,4} The two latter mechanisms are clearly observed in experiments with a free airfoil tip of significant sweep and loading, which is the case in the present work as detailed in section IV. The single-microphone measurements do not allow separating these contributions, which is a serious issue whenever more than one mechanism contribute.

The far-field microphone measurements still have the advantage of giving accurately access to the directivity of the radiated sound. Completing them with microphone-array localization techniques that can be used to discriminate the sources and to provide quantitative estimates of each of them is of primary interest. Yet the accuracy of such extractions and the practical issues inherent to the localization algorithms are seldom addressed in the literature. This is why microphone-array measurements recently performed in a previous work around a swept and loaded airfoil in clean flow and in a turbulent stream are re-examined in this paper to illustrate a relevant procedure,^{3,4} also referring to analytical source models for a better interpretation of the microphone-array output.

The initial motivation of the previous work was to address all broadband-noise mechanisms involved in counter-rotating open rotors (CROR).^{3,4} For this the classical set-up including a rectangular airfoil held between two end-plates was considered as too limiting, even if many reliable results have been obtained this way in the literature of airfoil noise and of its analytical predictions.⁵ The aerodynamic noise generation for a finite-span airfoil involves more features^{6,7} and additional noise sources such as airfoil tip can contribute to the process.⁸ Previous investigation of the wall-mounted finite length airfoil with flat ended tip was done by Moreau *et al.*^{6,7} The present contribution brings new insight into the topic. The results of the source localization with the beamforming method pointed the existence of a junction noise source at low frequencies, increasing with the angle of attack, a trailing-edge noise source dominating at middle frequencies for low angles of attack and a trailing-edge tip source observed at high frequencies.

The present contribution is part of the research program of the industrial aeroacoustic chair ADOPSYS agreed between the French Research Agency (ANR), SAFRAN Aircraft Engines and the Laboratoire de Mécanique des Fluides et d'Acoustique (LMFA) of Ecole Centrale de Lyon (ECL). The acoustic and aerodynamic measurements for a wall-mounted finite-span swept airfoil were conducted and some results were presented by Giez *et al.*^{3,4} In the continuation of these measurements an advanced analysis of the source localization results is proposed. The deconvolution method called CIRA⁹ is used to calculate the power of individual noise sources that could not be separated from far-field single-microphone measurements. The Bayesian inference¹⁰ algorithm based on the Bayes rule is presented as well and allows to include the coherence of the sources into the reconstruction process. Beyond the need to properly characterize the individual sources and their ranking as a function of the configuration, the study is also aimed at building a data base for each of them in view of the validation of prediction methods, in particular analytical ones.

I. Experimental Setup

The experiments are carried out in the open-jet anechoic wind tunnel of Ecole Centrale de Lyon with a converging nozzle with a 300 mm × 400 mm rectangular section. The flow is delivered by a subsonic centrifugal fan and the residual turbulence intensity is 0.5%. An additional grid that generates a turbulence intensity of 8% is used to investigate turbulence-impingement noise more specifically. The flow speed ranges from 30 m/s to 100 m/s (chord-based Reynolds numbers from 2.9×10^5 to 11×10^5 , maximum Mach number close to 0.3).^{3,4}

A swept cambered airfoil of chord length 150 mm, span length 250 mm, sweep angle 35° and relative thickness 4% with free tip is mounted on a single end-plate. A rotating disk allows varying the geometrical angle of attack from 0° to 11°. The airfoil/plate junction at leading edge is located 200 mm downstream of the wind-tunnel nozzle, and the whole mock-up is embedded well inside the potential core of the jet so that the direct interaction with the upper free shear layer is avoided. Far-field single-microphone measurements are made normal to the mockup at 2 m away from the leading edge in the mid-span plane. A piezotronic type 426B03 quarter-of-an-inch microphone was used.

The microphone array used for source localization is made of 81 digital MEMS microphones arranged in a 9-arm spiral structure (figure 1). It is placed at a normal distance of 50 cm from the airfoil out of the flow (figure 2). The localization is made on both airfoil sides: the left-bank side (facing the suction side of the airfoil) and the right-bank side (facing the pressure side). For each experimental configuration the signals of all probes are simultaneously recorded by the multi-channel acquisition system. It is worth noting that the far-field measurements and source localisation measurements were not conducted simultaneously. So the

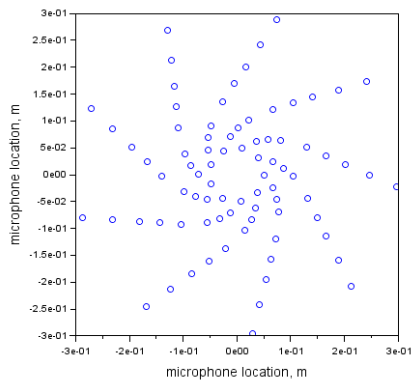


Figure 1: Scheme of the microphone array.

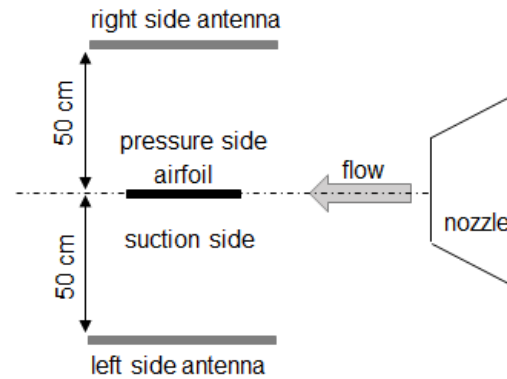


Figure 2: Scheme of the experimental set up for the source localization study.

microphone array did not influence the far-field acoustic measurements.

The use of MEMS microphones in a flat array raises a necessary high frequency artefact. Microphones are mounted in a small cavity that induces a resonance around 20 kHz. This effect has been pointed out by Humphreys.¹¹ The resonance needs to be corrected *via* a calibration procedure. A typical microphone response curve is presented in figure 3, showing the resonance in the high-frequency range. This curve is a mean calibration over the microphones and is valid up to 20 kHz.

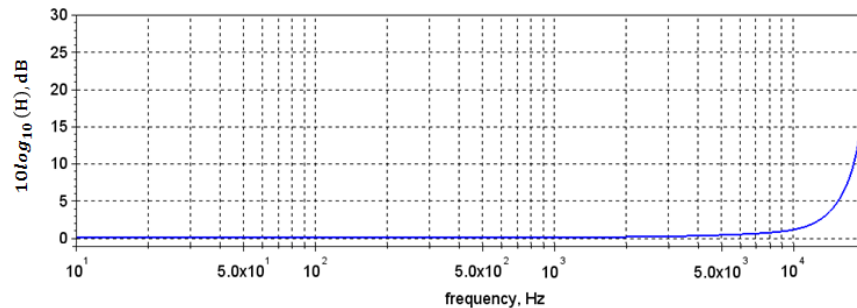


Figure 3: Typical response curve of a microphone of the antenna, showing the high-frequency resonance.

II. Analytical Model of Leading-Edge Noise

Analytical models, if available, provide a clear understanding of basic features that help to interpret the localization results. Up to that point Amiet's model of sound generation by impingement of vortical disturbances on a leading edge is discussed in this section, mostly in connection with high-frequency airfoil noise sources. Such sources are clearly apparent in the source maps produced by the microphone-array post-processing in the present study with grid-generated turbulence. Yet they can hardly be extracted from the background noise in the high-frequency part of the spectrum when investigated with a single far-field microphone.

Amiet's model of turbulence-impingement noise at a leading edge is referred to here because it has proven its efficiency in predicting the broadband noise of thin airfoils. For convenience it is first considered in a two-dimensional context, assimilating the airfoil to a thin rigid segment of chord c embedded in a parallel uniform mean flow of speed U_0 . The model allows deriving a closed-form expression for the unsteady lift $\ell(y_1)$ distributed along the airfoil by making use of Schwarzschild's technique.^{12,13} This distribution corresponds to perfectly correlated sources along the chord at any considered frequency. It reads

$$\ell(y_1) = \frac{2\rho_0 U_0 w e^{i\pi/4}}{\sqrt{\pi(1+M_0)} k_1 y_1} e^{i(1-M_0) \frac{kc}{2\beta^2} (1+2y_1/c)} \quad (1)$$

$$\times \left\{ 1 - \sqrt{\frac{2}{1+2y_1/c}} - E\left(\frac{kc}{\beta^2}(1-2y_1/c)\right) \right\}$$

in which y_1 is the chordwise coordinate with origin at mid-chord, ρ_0 and U_0 are the mean fluid density and speed, w is the amplitude of the incident velocity fluctuations at angular frequency ω , $k = \omega/c_0$ and $k_1 = \omega/U_0$ are the acoustic and aerodynamic wavenumbers respectively, $M_0 = U_0/c_0$ and $\beta^2 = 1 - M_0^2$. E is the Fresnel integral

$$E(\xi) = \int_0^\xi \frac{e^{it}}{\sqrt{2\pi\xi}} d\xi$$

The expression states that equivalent sources are distributed all along the flat plate and that their amplitude decreases from the edge with the inverse square-root singularity and goes to zero at the trailing edge by virtue of the Kutta condition. Despite this distributed character expected from the general background of the acoustic analogy,¹⁴ the conversion of vortical disturbances into sound physically takes places in the very vicinity of the leading edge.

In two dimensions the radiation of the lift distribution can be computed numerically by making the scalar product with the normal derivative of the two-dimensional free-space Green's function in a uniformly moving fluid. This function, with the present convention $e^{i\omega t}$ for the time Fourier transform, is written as

$$G(\mathbf{x}, \mathbf{y}) = \frac{i}{4\beta} e^{-ikM_0(x_1-y_1)/\beta^2} H_0^{(1)}\left(\frac{kr_s}{\beta^2}\right) \quad (2)$$

with $r_s^2 = (x_1 - y_1)^2 + \beta^2(x_2 - y_2)^2$. Here $\mathbf{x} = (x_1, x_2)$ is the observer point and $\mathbf{y} = (y_1, y_2 = 0)$ is the source point.

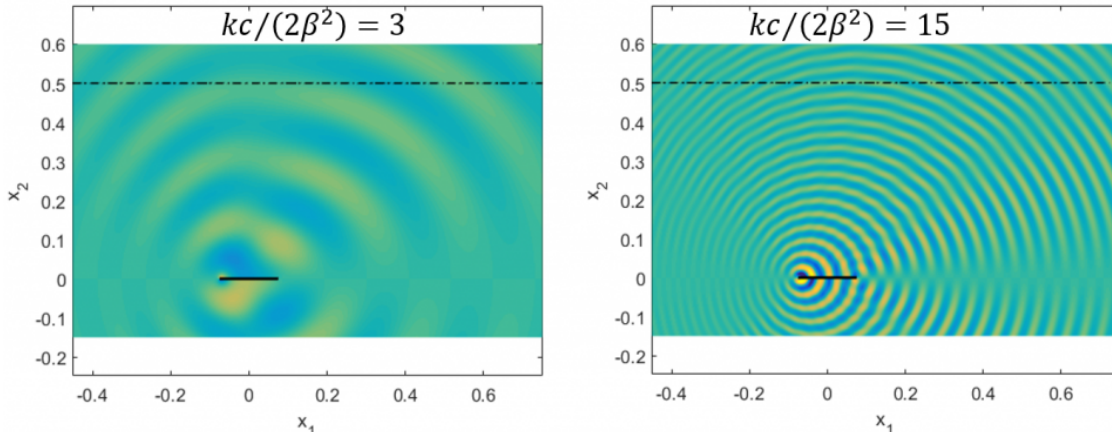


Figure 4: Maps of typical instantaneous acoustic pressures radiated by an airfoil according to 2D Amiet's model. High-frequency regime, 2 kHz (left) and 10 kHz (right). $c = 15$ cm, $U_0 = 90$ m/s. Typical array location along the dashed-dotted line.

Typical instantaneous pressure fields reconstructed this way are shown in figure 4. At 2 kHz examination of the wavefront structure suggests that an algorithm based on distributed uncorrelated monopoles will not precisely localize the source. At 10 kHz the sound obviously originates from the leading edge, even if the equivalent source is not a concentrated monopole; this explains why a source will be located at the edge by the microphone-array post-processing.

It must be noted that the convection effect and the refraction that occurs across the shear-layers of the wind-tunnel jet (not accounted for in figure 4) are corrected in the post-processing described in section III.

Another interest of Amiet's model is that it provides an expression for the far-field sound pressure PSD. In the simple case of a rectangular airfoil of large aspect ratio and for an observer in the mid-span plane,

this PSD reads

$$S_{pp}(\vec{x}, \omega) = \left(\frac{\rho_0 k c x_3}{2 S_0^2} \right)^2 \pi U_0 \frac{L}{2} \Phi_{ww}(k_1, 0) |\mathcal{L}(x_1, k_1, 0)|^2, \quad (3)$$

with

$$\Phi_{ww}(k_1, 0) = \frac{U_0}{\pi} S_{ww}(\omega) l_y(\omega), \quad k_1 = \frac{\omega}{U_0},$$

where $S_{ww}(\omega)$ is the upwash-velocity spectrum and $l_y(\omega)$ the associated correlation length. \mathcal{L} is an analytical transfer function, not detailed here. An extended version of this result accounting for sweep and other details are given in Giez *et al*^{3,4} but this is not essential for the present discussion. It is enough to retain that the statistical quantities S_{ww} and l_y of the incident turbulence determine the sound radiation. Once the complementary streamwise velocity spectrum S_{uu} is measured by hot-wire anemometry and properly fitted by a von Kármán or Liepmann model, an estimation of S_{ww} is obtained and sound predictions can be made. The fitting generates values of the turbulent intensity and of the integral length scale Λ that are of 8 % and 2 cm in the present experiment, respectively. $l_y(\omega)$ is deduced from Λ . Paterson & Amiet⁵ pointed that the spanwise correlation length of the induced lift on the airfoil is larger than the correlation length of the turbulence by typically a factor of about 1.6. Combined with the effect of sweep this makes a factor of 2 reasonably expected in the present case.

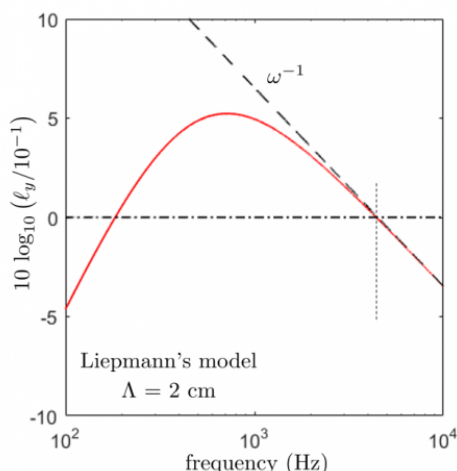


Figure 5: Estimated spanwise correlation length compared to the microphone-array discretization step of 1 cm.

The integral length scale Λ is of 2 cm, which leads to the estimated spanwise correlation length reported in figure 5. More precisely this length is made dimensionless by the 1 cm discretization step of the localization map detailed later on and expressed in equivalent decibels. This rough analysis suggests that beyond 4 kHz the correlation length is smaller than the discretization step. This also occurs below 200 Hz but at so low frequencies the localization goes less accurate. As long as the discretization step is larger than the correlation length, assuming uncorrelated cells in the localization is relevant. Therefore the source quantification can be used to reconstruct the far field in a convincing way, as presented in the next section. In contrast at frequencies for which the step is smaller than the correlation length, relying on the localization leads to underestimate that length and thus also the sound according to equation (3). When the ratio plotted in figure 5 is positive it corresponds to the expected amount of underestimation and its value can be used to somewhat empirically correct the transposed spectrum.

III. Post-Processing Techniques

Three existing sound source localisation algorithms are used in the present investigation: the conventional beamforming, a deconvolution method called CIRA⁹ and the Bayesian algorithm. The conventional beamforming is a robust method used as the reference processing in the sound source localization community. However, it has some significant drawbacks which motivate the development of more advanced methods.

The first limit is the low spatial resolution in the low-frequency range. The second and most important one is the presence of side-lobes that can modify the focused level leading to bias of the beamforming maps. Therefore in the case of multiple sources the conventional beamforming can be used to localize sources but not to properly quantify them.

The algorithm CIRA has been developed in 1994 by ONERA. It belongs to the family of deconvolution methods and is very similar to DAMAS in the problem formulation. The solution is sought using a steepest gradient descent instead of a Gauss-Seidel procedure. Details of the algorithm are given in section III.B. The algorithm CIRA is free from aforementioned disadvantages. It provides a better resolution at low frequencies. It also allows separating several sources from each other and computing a relevant power level spectrum for each. However, as the deconvolution is an iterative method, the computations take much more time than for beamforming. A decorrelation assumption between point sources is used in this algorithm.

The Bayesian inference (BI) algorithm was proposed by Antoni¹⁰ and is based on a statistical approach to the sound source reconstruction problem. This method belongs to the family of inverse array methods¹⁵ because it makes use of regularized matrix pseudo-inversion. A particular aspect of the Bayesian inference is the ability to include for *prior* information on the solution in a solid mathematical framework. For instance it is possible to account the *prior* knowledge on the source position or on the source correlation property (such as a correlation length), using the source covariance matrix $\mathbf{\Omega}_{\mathbf{q}}$ (see section III.C). Similarly known properties of the noise can also be included using the noise covariance matrix $\mathbf{\Omega}_{\mathbf{b}}$. Another specific aspect of the BI is the decomposition of the source field onto geometry-dependent spatial basis functions. As near field holography uses plane waves to study vibrating plates or cylindrical holography uses cylindrical harmonics to study jet noise, the BI offers the possibility to automatically tune the spatial basis to the geometry, making this method a very versatile tool.

The calculations have been done for 5-seconds signals at frequencies ranging from 0.2 kHz to 20 kHz. The frequency resolution is 10 Hz with a sample overlap of 50%. The cell of the calculation grid has a size of 0.01 m.

III.A. Beamforming Algorithm

For the number- m sensor the pressure signal p_{mi} generated by the assumed source of number i at angular frequency ω reads

$$p_{mi}(\omega) = h_{mi}(\omega)A_i(\omega) \quad (4)$$

where $A_i(\omega)$ is an amplitude factor and $h_{mi}(\omega)$ is a steering function representing the acoustic propagation. In the case of a monopole source in free field without flow $h_{mi}(\omega)$ can be expressed as (for the convention $e^{-i\omega t}$)

$$h_{mi}(\omega) = \frac{e^{ikr}}{r} \quad (5)$$

In the present application, the source to microphone distance r is modified to account for flow convection in a formulation based on Elias.¹⁶

The cross-spectral matrix (CSM) formulation for pairs of sensors m and n is obtained as

$$P_F^2(\omega) = \frac{\sum_m^M \sum_n^M h_{mi}(\omega)S_{mn}(\omega)h_{ni}^*(\omega)}{\sum_m^M \sum_n^M |h_{mi}(\omega)|^2|h_{ni}(\omega)|^2} \quad (6)$$

where $P_F^2(\omega)$ is the mean quadratic pressure of the beamformed signal at scan point, $S_{mn}(\omega)$ is the cross-spectrum between sensors m and n . The model of the cross-spectrum assumes a single monopole of amplitude $A(\omega)$ and free-field spherical wave propagation. Now

$$S_{mn}(\omega) = A(\omega)^2 h_{mi}^*(\omega)h_{ni}(\omega) \quad (7)$$

so the focused point level computed from Eq. (6) at the source location reads

$$P_F^2(\omega) = \frac{\sum_{m=1}^M \sum_{n=1}^M A(\omega)^2 |h_{mi}(\omega)|^2 |h_{ni}(\omega)|^2}{\sum_{m=1}^M \sum_{n=1}^M |h_{mi}(\omega)|^2 |h_{ni}(\omega)|^2} = A(\omega)^2 \quad (8)$$

In order to ensure a correct amplitude definition the following conditions should be met:

- only one source exists;
- the source directivity function and the acoustic propagation function correspond to a model monopole;
- the position of the source corresponds to the location of the focused point.

When several sources are investigated, this method cannot give the quantification of each source due to the fact that interference terms between sources are not taken into account. In other words, the beamforming is processed at each focusing point independently as if there was only one source on each focusing point. The deconvolution method CIRA is used as an alternative in the next section. Equation (6) is sensitive to microphone uncorrelated noise (terms $m = n$). The diagonal of the CSM in equation 6 can be ignored so that the effect of hydrodynamic noise of the shear layer on the microphones is reduced. A second improvement which is applied in the following is the possibility to take into account the convection and the refraction effect of the flow in the model (equation 5).

III.B. CIRA Algorithm

The deconvolution method CIRA⁹ is an iterative method that takes the results of beamforming as an input. For N multiple sources equation (4) is extended as

$$p_m(\omega) = \sum_i^N p_{mi}(\omega) = \sum_i^N h_{mi}(\omega)A_i(\omega) \quad (9)$$

The detailed description of the method is given by Piet *et al.*⁹ It is based on the averaged cross-spectrum

$$\begin{aligned} S_{mn} &= \langle p_m^* p_n \rangle = \left\langle \left(\sum_i^N h_{mi}(\omega)A_i(\omega) \right)^* \left(\sum_j^N h_{nj}(\omega)A_j(\omega) \right) \right\rangle \\ &= \sum_i^N \sum_j^N h_{mi}(\omega)^* h_{nj}(\omega) \langle A_i(\omega)^* A_j(\omega) \rangle \end{aligned} \quad (10)$$

The assumption is made that all N equivalent monopole sources are uncorrelated or $\langle A_i^*(\omega)A_j(\omega) \rangle = 0$ if $i \neq j$ so that $S_{mn}(\omega) = \sum_i^N h_{mi}(\omega)^* h_{ni}(\omega) |A_i(\omega)|^2$. The output of the beamforming will be

$$P_j^2(\omega) = \frac{\sum_m^M \sum_n^M \sum_i^N h_{mj}(\omega) h_{mi}^*(\omega) h_{ni}(\omega) h_{nj}^*(\omega) |A_i(\omega)|^2}{\sum_m^M \sum_n^M |h_{mj}(\omega)|^2 |h_{nj}(\omega)|^2} = \sum_i^N H_{ij} |A_i(\omega)|^2 \quad (11)$$

Equation (11) can be written in the matrix form

$$\mathbf{B} = \mathbf{H}\mathbf{S} \quad (12)$$

where \mathbf{B} is a column vector of dimension $[N, 1]$ filled with the beamforming outputs $B_j = P_j^2$, \mathbf{H} is the array response matrix of dimension $[N, 1]$ and of elements H_{ij} and \mathbf{S} is the source column vector of dimension $[N, 1]$ made of source squared amplitudes $S_i = |A_i|^2$.

The solution of equation (12) can be found by iteration. The initialization is $S_i = 0$ for all sources i . At each k iteration the first step is to compute the error vector between the initial beamforming map \mathbf{B} and the beamforming map $\mathbf{H}\mathbf{S}_{(k-1)}$ produced by the source distribution found at the previous iteration:

$$\bar{\mathbf{E}}_{(k)} = \mathbf{B} - \mathbf{H}\mathbf{S}_{(k-1)} \quad (13)$$

Then the solution is upgraded from the computed error:

$$\mathbf{S}_{(k)} = \mathbf{S}_{(k-1)} + \mu \bar{\mathbf{E}}_{(k)} \quad (14)$$

where μ is the convergence parameter which controls the weight given to the error in the solution upgrade. It ensures the algorithm stability. Computations are stopped when the threshold for the relative error (10^{-4}) is approached or when a large number of iterations (1000) have been computed.

III.C. Bayesian Algorithm

Assuming that a decomposition basis is available, the Bayesian Inference (BI) technique expresses the inverse problem in a standard form

$$\mathbf{y} = \hat{\mathbf{S}}\mathbf{c} \quad (15)$$

where \mathbf{y} is the coordinate vector in an optimal basis of the measurement vector \mathbf{p} ; \mathbf{c} is the vector of source coefficients expressed in this basis and $\hat{\mathbf{S}}$ is the propagation operator matrix which turns out to be a diagonal matrix. This is not a coincidence, since the optimal basis in the Bayesian sense has been specifically designed to have this property.¹⁰ The solution is computed with a Tikhonov regularization.

To compute the optimal basis, a singular-value decomposition (SVD) is operated on the propagation operator \mathbf{G} whitened by the two covariance matrices: $\Omega_{\mathbf{b}}^{-1/2}\mathbf{G}\Omega_{\mathbf{q}}^{-1/2} = \hat{\mathbf{U}}\hat{\mathbf{S}}\hat{\mathbf{V}}^*$. Then the transfer matrix Φ from the source physical space to the optimal space is computed using

$$\Phi = \Omega_{\mathbf{q}}^{-1/2}\mathbf{G}^*\hat{\mathbf{S}}^{-1}\Omega_{\mathbf{b}}^{-1/2}\hat{\mathbf{U}} \quad (16)$$

The solution $\tilde{\mathbf{q}}$ is computed from the estimate $\tilde{\mathbf{c}}$ in this optimal space by $\tilde{\mathbf{q}} = \Phi\tilde{\mathbf{c}}$. Similarly, the coordinates of the measurement vector in this reference frame are computed using

$$\mathbf{y} = \hat{\mathbf{U}}^*\Omega_{\mathbf{b}}^{-1/2}\mathbf{p} \quad (17)$$

The most probable solution $\tilde{\mathbf{q}}$ is the source distribution which provides the best compromise between the fidelity to the noisy measured data \mathbf{p} and the prior information $\Omega_{\mathbf{q}}$.

It is possible to force the sparsity of the solution using an iterative approach, just as deconvolution algorithms iterate on the beamforming maps. The idea is to use the solution $\tilde{\mathbf{q}}_i$ of a previous iteration as a prior in the source covariance matrix $\Omega_{\mathbf{q}}$. The solution is not only sparser but also less directive since interaction between equivalent point sources is limited. In the higher frequency range, where the single iteration BI tends to provide “hyper-directive” solutions towards the array, the iterative BI can lead to a better recovery of a witness far-field microphone spectrum.

IV. Source Localization Results

The beamforming technique applied in the previous work showed that several noise sources can be observed depending on the configuration and the frequency range:

- the interaction with the boundary layer at the junction of the airfoil with the plate,
- the airfoil tip section where the tip vortex develops,
- the leading-edge impingement of turbulence,
- the scattering of boundary-layer turbulence at the trailing edge,
- special sources associated with the formation of a leading-edge vortex.

Various configurations were selected to characterize each source. The most detailed investigation was done with the CIRA method, which allows to separate the sources and to obtain quantitative estimates of the associated spectra. The acoustic levels are presented with respect to some reference level (RL).

Figure 6 shows the localization maps calculated by the conventional beamforming and by the CIRA method for the configuration at 9° angle of attack and 90 m/s with the residual 0.5% turbulence. At low frequencies the CIRA method performs much better to identify the noise source at the tip. This configuration also has noise sources at the junction, at the leading and trailing edges and at the trailing-edge tip corner. The unexpected shift of the trailing-edge noise source as viewed from the suction side was observed despite wind tunnel corrections, whereas the localization as viewed from the pressure side seems more accurate and reliable. This problem is currently under investigation.

The scanned plane was sub-divided into 8 zones: 4 for the leading edge area and 4 for the trailing edge area, as shown in figure 7 by the rectangular boxes. This allows analyzing the contribution of each source in the airfoil self-noise configuration, presuming that each zone is dominated by only one source, by comparing the associated pressure spectra.

The following formula is used to convert the sound power levels (SWL) produced by the localization algorithm into sound pressure levels (SPL) in dB:

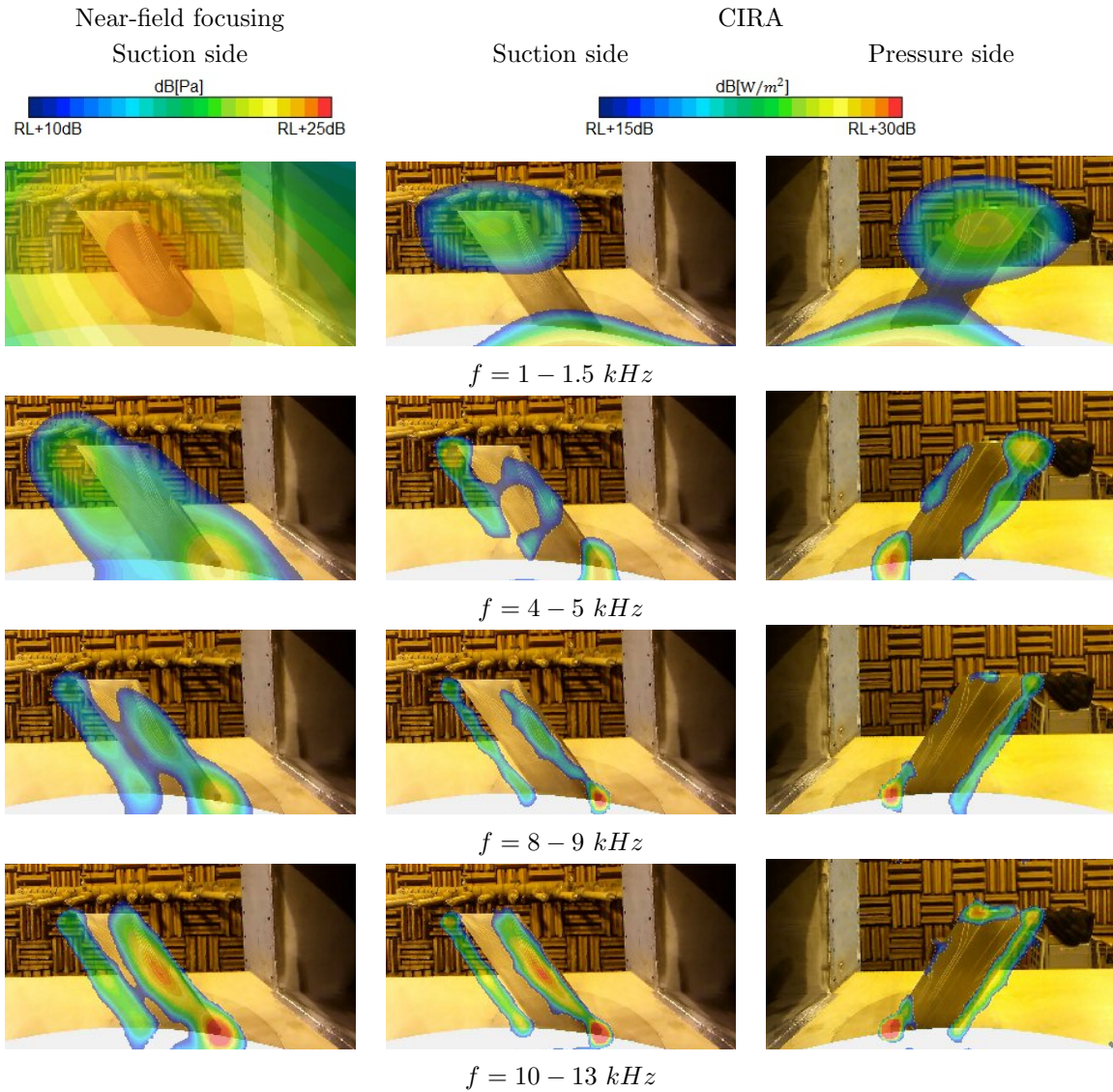


Figure 6: Source localization maps at $\alpha = 9^\circ$ and 90 m/s. Residual turbulence 0.5% (clean flow). RL stands for a common reference level.

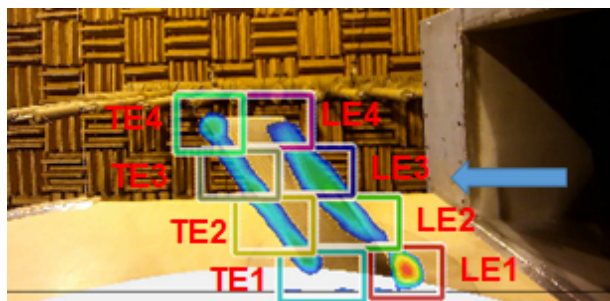


Figure 7: Picture of the swept airfoil and localization map. Zones for the extraction of the SPL. LE - leading edge; TE - trailing edge. Nozzle exit on the right.

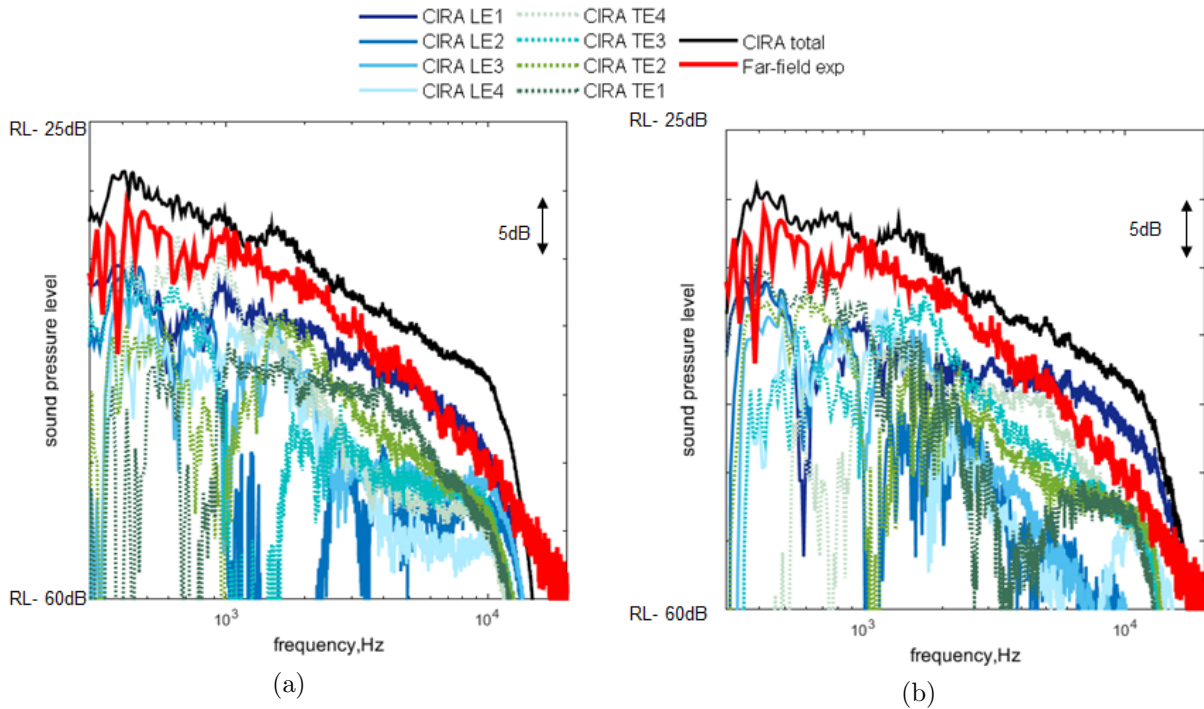


Figure 8: SPL spectra for 8 zones on the suction side (a) and on the pressure side (b) produced by the CIRA method. Airfoil at $\alpha = 9^\circ$ and $U_\infty = 90 \text{ m/s}$. Turbulence rate 0.5%.

$$L_p = L_w - 10 \log_{10} \left(\frac{A}{A_0} \right) \quad (18)$$

where L_p is the SPL, L_w is the SWL, $A = 4\pi r^2$ is the area of the sphere of radius $r = 2 \text{ m}$ (distance from the airfoil to the far-field microphone in the present case) and A_0 is the reference area 1 m^2 .

Equation (18) is an approximation since propagation effects are not included: flow convection, reflection on the mounting plate and nozzle diffraction. Moreover, the CIRA method does not reconstruct source directivity effects.

Figure 8 compares the obtained SPL spectra for each zone, the total recombined spectrum (black line) and the measured far-field spectrum (red line) after extraction of the background noise. The recombined spectrum of all zones produced by the CIRA method overestimates the measured far-field spectrum by a couple of dB. The differences at higher frequencies around 10 kHz are more than 5 dB. The origin of the discrepancies is presently investigated, based on spanwise-correlation arguments.

At frequencies beyond 2 kHz the source at the junction (zone LE1) dominates for both sides of the array. For the pressure side the trailing-edge tip contributes at frequencies from 2.5 kHz to 6 kHz. Trailing-edge noise as viewed from this side is more significant than leading-edge noise.

An interesting feature is the imbalance between sounds radiated at high frequencies (typically in the range 10-13 kHz) from the leading-edge area on the suction side and on the pressure side. This suggests that the source is not exactly at the edge, as what would be the case for turbulence impingement. In fact this behaviour is attributed to the formation of a leading-edge vortex that separates from the leading edge and reattaches slightly farther downstream.^{3,4}

Figure 9 presents localization maps from the array facing the suction side of the airfoil at $\alpha = 4^\circ$ and 90 m/s. A source at the trailing-edge tip corner is clearly found in this case at frequencies from 13 kHz to 20 kHz, caused by a probable interaction of the unsteady tip vortex with this part of the surface.

Figure 10 shows SPL spectra for the same case. The far-field spectrum is again overestimated by the reconstruction, as in the previous case (around 5 dB differences). It is worth noting that both measured and reconstructed far-field spectra exhibit a high hump at frequencies from 10 kHz to 16 kHz. The hump of the directly measured spectrum is more clearly divided into two peaks. The zones TE4 and TE3 contribute to the first peak, whereas the second one fully corresponds to the TE4 zone (trailing-edge tip source).

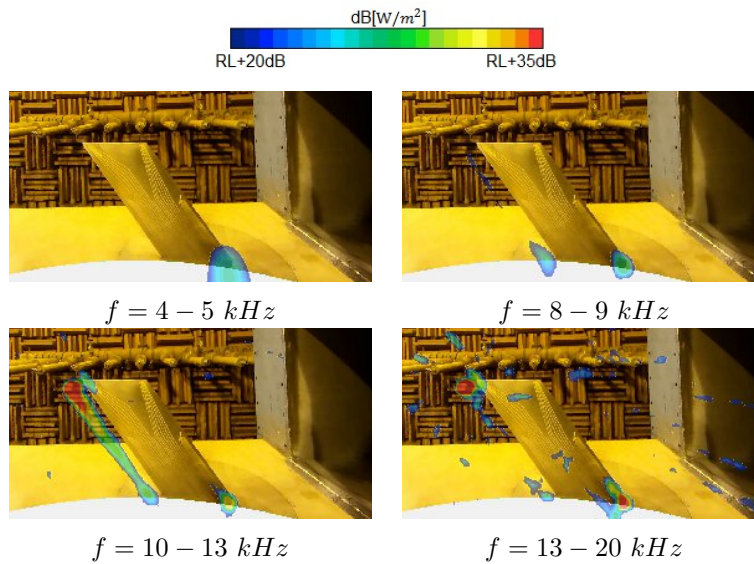


Figure 9: Source localization maps at $\alpha = 4^\circ$ and 90 m/s. Turbulence 0.5%. CIRA. Suction-side view.

Figure 11 presents SPL spectra for arrays facing the suction (a) and pressure (b) sides of the airfoil in the configuration at 9° and 90 m/s with the high turbulence intensity of 8%. At frequencies below 3 kHz the differences are quite important but now the SPL calculated from the CIRA technique underestimates the measured far-field spectrum. At higher frequencies a very good agreement is found, especially on the pressure-side position. In this case the physics of the leading-edge vortex is probably overwhelmed by the incoming turbulence and turbulence-impingement noise, known to be symmetrically radiated, clearly dominates.

The discrepancies at frequencies below 3 kHz can be associated with the assumption of the perfectly decorrelated sources made for the CIRA model. The correlation length of the pressure fluctuations at

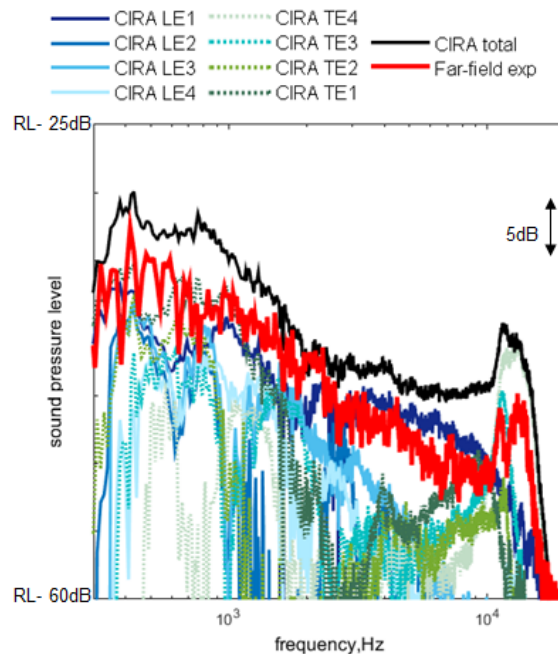


Figure 10: SPL spectra for 8 zones on the suction side produced by the CIRA method. Airfoil at $\alpha = 4^\circ$ and $U_\infty = 90$ m/s. Turbulence rate 0.5%. Suction side.

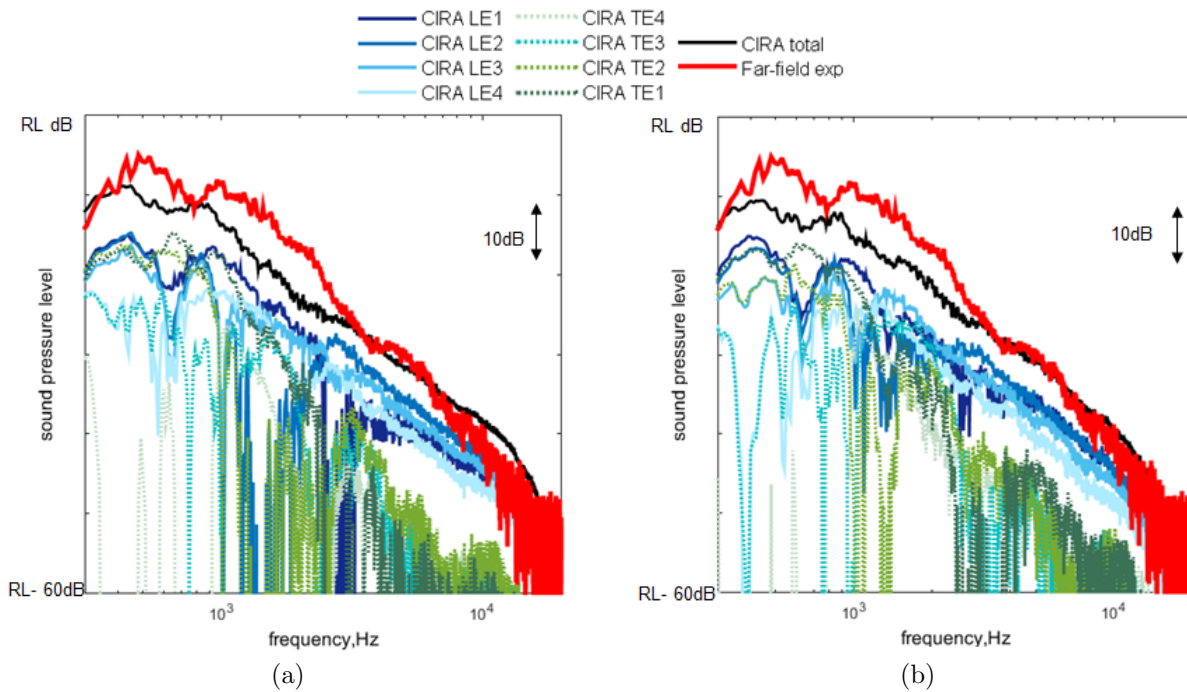


Figure 11: SPL spectra for 8 zones on the suction side (a) and on the pressure side (b) produced by the CIRA method. Airfoil at $\alpha = 9^\circ$ and $U_\infty = 90 \text{ m/s}$. Turbulence rate 8%.

frequencies below 3 kHz reaches 0.02 m whereas as was mentioned before, the cell size of the calculation grid is 0.01 m. If a correction is applied according to the positive range in figure 5, a very good agreement is found over the entire frequency range. To avoid corrections, the iterative Bayesian focusing method¹⁰ when the sources are assumed to be partially correlated was used to improve the results. The iterative version of the BI with 30 iterations has a better resolution than the original one due to the source sparsity. The obtained spectrum (figure 12 blue line) is in a good agreement with the measured one (red line) starting from 1500 Hz. At high frequencies (from 8 kHz) the spectrum reconstructed with the BI starts to increase.

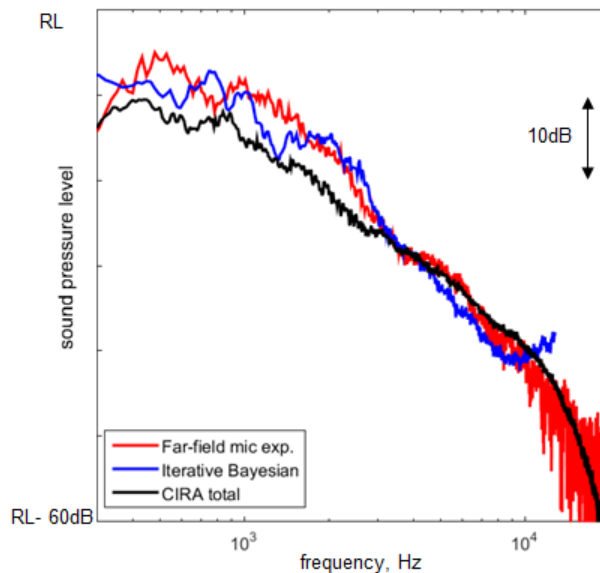


Figure 12: Comparison of SPL spectra for the airfoil at $\alpha = 9^\circ$ and $U_\infty = 90 \text{ m/s}$. Turbulence rate 8%. Pressure side.

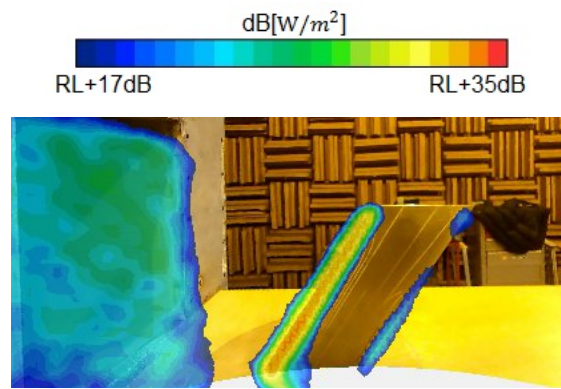


Figure 13: Source localization map at $\alpha = 9^\circ$ and 90 m/s calculated with the CIRA method. Residual turbulence 8%. Frequency range from 10kHz to 13kHz. RL stands for a common reference level.

Overall the Bayesian algorithm reduces the discrepancies from 10 dB to 5 dB compared with the CIRA method.

Figure 13 demonstrates the source localisation map for the aforementioned case with turbulence rate 8% where at high frequencies a weak source along the trailing edge is also observed.

Conclusion

The present work is a re-examination of microphone-array measurements performed in a previously reported experimental investigation^{3,4} initially dedicated to the turbulence-impingement noise of an airfoil in realistic loading conditions. A more detailed analysis has been made, based on localization results obtained by putting the array on both sides of the airfoil outside the flow.

Furthermore, because of the presence of several combined noise sources, the classical beamforming gives only qualitative results. Therefore the deconvolution method CIRA has been applied to produce quantitative information. The area around the airfoil was divided into eight zones which correspond to the most expected sources: leading-edge junction, leading-edge vortex, leading and trailing edge tips and trailing edge. For each zone the contribution to the sound pressure level was calculated as well as spectra for all zones. The total reconstructed spectra were compared with the measured far-field spectra. A good overall agreement has been obtained but either underestimates or overestimates of the far-field sound (differences around 10 dB) are observed with the reconstruction procedure.

Some discrepancies were assumed to be caused by the uncorrelated source model used in the CIRA. To check this idea the Bayesian inference algorithm has been used where the correlation length is included. The obtained reconstructed spectrum has provided a better agreement with the measured one at mid frequencies (discrepancies around 5 dB). An analytical turbulence-impingement noise model confirmed that the discrepancies are related to correlation-length issues. This suggests that the array post-processing still needs to be improved to provide accurate spectral information about extracted sources. Actions on the basic source models and on their correlation properties are presently investigated for this goal.

Acknowledgment

This work was performed within the framework of the Labex CeLyA of the Université de Lyon, within the program “Investissements d’Avenir” (ANR-10-LABX-0060/ANR-11-IDEX-0007) operated by the French National Research Agency (ANR) and is also supported by the industrial Chair ADOPSYS co-financed by Safran Aircraft Engines and the ANR (ANR-13-CHIN-0001-01).

References

- ¹Roger, M. and Moreau, S., “Broadband self noise from loaded fan blades,” *AIAA journal*, Vol. 42, No. 3, 2004, pp. 536–544.
- ²Moreau, S. and Roger, M., “Effect of airfoil aerodynamic loading on trailing edge noise sources,” *AIAA journal*, Vol. 43,

No. 1, 2005, pp. 41–52.

³Giez, J., Vion, L., Roger, M., and Moreau, S., “Effect of the Edge and Tip Vortex on Airfoil Self Noise and Turbulence Impingement Noise,” *22nd AIAA/CEAS Aeroacoustics Conference*, No. 2996, Lyon, France, May 2016.

⁴Giez, J., Vion, L., Roger, M., Yakhina, G., and Moreau, S., “Effects of Intermittency and Geometry on the Turbulence Impingement Noise of a CROR Rear-Rotor Blade,” *23rd AIAA/CEAS Aeroacoustics Conference*, No. 3217, Denver, USA, June 2017.

⁵Paterson, R. and Amiet, R., “Acoustic radiation and surface pressure characteristics of an airfoil due to incident turbulence,” *3rd Aeroacoustics Conference*, 1976, p. 571.

⁶Moreau, D., J., Doolan, C., J., Alexander, W., N., Meyers, T., W., and Devenport, W., J., “Wall-mounted finite airfoil-noise production and prediction,” *AIAA Journal*, Vol. 54, No. 5, 2016, pp. 1637–1651.

⁷Moreau, D. J. and Doolan, C. J., “Tonal noise production from a wall-mounted finite airfoil,” *Journal of Sound and Vibration*, Vol. 363, 2016, pp. 199–224.

⁸Brooks, T. F. and Marcolini, M. A., “Airfoil tip vortex formation noise,” *AIAA journal*, Vol. 24, No. 2, 1986, pp. 246–252.

⁹Piet, J. and Elias, G., “Modélisation du champ acoustique incident sur la coiffe d’Ariane 5 par des sources simples,” *Office national d’études et de recherches spatiales*, 1994.

¹⁰Antoni, J., “A bayesian approach to sound source reconstruction: Optimal basis, regularization, and focusing,” *The Journal of the Acoustical Society of America*, Vol. 131, No. 4, 2012, pp. 2873–2890.

¹¹Humphreys, W., Shams, Q., Graves, S., Sealey, B., Bartram, S., and Comeaux, T., “Application of MEMS microphone array technology to airframe noise measurements,” *11th AIAA/CEAS Aeroacoustics Conference*, 2005, p. 3004.

¹²Amiet, R. K., “High frequency thin-airfoil theory for subsonic flow,” *AIAA journal*, Vol. 14, No. 8, 1976, pp. 1076–1082.

¹³Roger, M. and Moreau, S., “Back-scattering correction and further extensions of Amiet’s trailing-edge noise model. Part 1: theory,” *Journal of Sound and Vibration*, Vol. 286, No. 3, 2005, pp. 477–506.

¹⁴Williams, J. F. and Hawkings, D. L., “Sound generation by turbulence and surfaces in arbitrary motion,” *Philosophical Transactions of the Royal Society of London A: Mathematical, Physical and Engineering Sciences*, Vol. 264, No. 1151, 1969, pp. 321–342.

¹⁵Finez, A., Picard, C., Le Magueresse, T., Leclere, Q., and Pereira, A., “Microphone array techniques based on matrix inversion,” *VKI Lecture Series STO-AVT-287*, 2017.

¹⁶Elias, G., “Évaluation des retards de propagation acoustique adaptée à la soufflerie sources CEPRA 19,” Tech. Rep. n° 38/3102 PN, Office national d’études et de recherches spatiales, 1993.